From scaled-up production of silicon-graphene nanocomposite to the realization of an ultra-stable full-cell Li-ion battery

2D Materials

OPEN ACCESS

RECEIVED
15 November 2020

REVISED
2 January 2021

ACCEPTED FOR PUBLICATION
28 January 2021

PUBLISHED
6 April 2021

PAPER

From scaled-up production of silicon-graphene nanocomposite to the realization of an ultra-stable full-cell Li-ion battery

Sara Abouali[1,2], Mohammad Akbari Garakani[1,2], Laura Silvestri[3], Eleonora Venezia[1], Luigi Marasco[1], Rosaria Brescia[4], Alberto Ansaldo[1], Michele Serri[1], Jaya Kumar Panda[2], Giammarino Pugliese[5], Elisa Mantero[1,2], Francesco Bonaccorso[1,2] and Vittorio Pellegrini[1,2]

[1] Graphene Labs, Istituto Italiano di Tecnologia, via Morego 30, 16163 Genova, Italy
[2] BeDimensional Spa, via Torrentesecca 3d, 16163 Genova, Italy
[3] Dipartimento di Tecnologie Energetiche, ENEA, C.R. Casaccia, Via Anguillarese 301, 00123 Roma, Italy
[4] Electron Microscopy Facility, Istituto Italiano di Tecnologia, Via Morego 30, 16163 Genova, Italy
[5] NanoChemistry, Istituto Italiano di Tecnologia, via Morego 30, 16163 Genova, Italy

E-mail: sara.abouali@iit.it **and** francesco.bonaccorso@iit.it

Keywords: silicon, graphene, nanocomposite anode, high capacity anode, Li-ion full cell

Supplementary material for this article is available online

Abstract

The realization of a high-performance Li-ion full-cell with an anode prominently based on silicon, which can surpass the energy densities of commercial graphite-based Li-ion batteries and cyclability compatible for industrial applications, is still a challenge. Here, we report a Li-ion full-cell that combines a silicon/graphene/carbon (Si/G/C) nanocomposite anodic material, with a commercial $LiNi_{0.33}Mn_{0.33}Co_{0.33}O_2$ (NMC_{111}) cathode. Using a pre-lithiation technique, the proposed Li-ion full-cell exhibits an energy density of ~400 Wh kg^{-1} at the electrode material level, with a capacity >1.6 mAh cm^{-2} and a capacity retention exceeding 90% after 300 cycles at C/2. These performances have been achieved by properly designing the anode material composed by Si nanoparticles wrapped by few-layer graphene flakes. An additional carbon coating is used to further improve the electron conductivity and mechanical integrity of the anodic structure upon charge/discharge cycles. The remarkable performance of the full-cell considering the scalability of the Si-based anode synthesis is a step forward towards the commercialization of high-capacity and high-energy density Li-ion batteries.

1. Introduction

Since the first commercial Li-ion batteries [1], strong efforts have been made to improve their specific capacities and specific energy densities, which led today to commercial Li-ion battery devices with a high energy density up to 250 Wh kg^{-1} [2]. Most of the commercial Li-ion batteries use graphite as the negative electrode and lithium cobalt oxide ($LiCoO_2$) as the positive one [1, 2]. Such active materials yield a limited theoretical capacity, which is becoming the limiting factor toward the development of higher capacity/energy density Li-ion batteries compared to the commercial standard [1–3].

To further improve the energy density of Li-ion batteries, silicon has long been considered as an ideal replacement for the graphite anode due to its high theoretical capacity of 4200 mAh g^{-1}, corresponding to the alloying reaction of Li and Si according to equation (1), which is far beyond the theoretical specific capacity of graphite (372 mAh g^{-1}) [4, 5]

$$Si + 4.4Li^+ + 4.4e^- \rightarrow Li_{4.4}Si. \quad (1)$$

However, upon alloying/de-alloying of Si with Li during charge/discharge cycles, Si undergoes a large volume change, which generates mechanical strain leading to the pulverization of the electrode, loss of electrical contact and consequently, poor electrochemical stability [5–7]. Several strategies have been investigated to overcome the aforementioned challenges [8]. In particular, it has been proposed the down-sizing of the bulk Si to nanosize structures to minimize the mechanical strains and cracking [9, 10] and tuning the properties of the slurry [11] and the

encapsulation of Si nanostructures in conductive carbon materials [12, 13]. The latter can simultaneously increase the electrical conductivity of the electrode and buffer the mechanical strains [12, 13]. In this context, several works were reported on the synthesis of Si/carbon composites including Si/graphite [14, 15], Si/reduced graphene oxide [16, 17], Si/3D graphene such as graphene aerogel [18] or graphene foam [19], Si/carbon nanotubes [20], Si/C core shell structures [21] and bio-inspired Si/carbon nanofibers [12, 22]. While great improvements have been reported over the years, most of the production methods reported so far for the most successful anodes are based on lab-scale approaches [23]. This implies the use of high raw material/manufacturing costs, which cannot be used for large-scale production, representing one of the main limitation for the industrial application of Si-based electrodes [8].

Among the different types of carbonaceous materials used, graphene-based materials is considered as an ideal additive for Li-ion battery electrodes [24–28] owing to its excellent electrical conductivity of ~2000 S cm^{-1} [24] and mechanical stability (Young's modulus of $E = 1.0 \pm 0.1$ TPa and intrinsic strength of 42 N m^{-1}) [27]. Additionally, the remarkable thermal conductivity of graphene (2000–4000 W m^{-1} K^{-1}) [29, 30] could be beneficial for heat dissipation in case of high-current loading (i.e. high C rates). In order to use graphene in real applications, however, it is essential to develop low-cost large-scale production routes to produce highly performing silicon-graphene composites [31]. To this end, we demonstrated the application of wet-jet milling (WJM) process to exfoliate layered materials such as graphite with a high potential for industrial production [32]. More recently, we also used the WJM technique to synthesize Si/few-layer graphene (FLG) composite that offers excellent performances as electrodes in Li-ion batteries [33, 34].

In addition to the aforementioned efforts on engineering the nanostructure of the electrode, the effect of the binder on the electrochemical performance and lifetime of the Si-based anodes has been reported [35]. Different types of water-based binders such as polyacrylic acid (PAA) [36, 37], carboxymethyl cellulose (CMC) [38], guargum [39] and alginate [40] have been reported. These polymeric binders contain abundant carboxylate and hydroxyl functional groups, which interact with Si particles through hydrogen bonding and/or covalent bonds and can effectively help to maintaining the integrity of the electrode by preventing the pulverization of the Si particles and consequently inhibit the capacity fading of the battery [41, 42].

Another serious issue originating from the huge volume changes of Si during alloying/de-alloying with Li, is the highly-unstable solid electrolyte interphase (SEI) [43, 44]. As the Si particle undergoes expansion and contraction, the SEI layer easily cracks and breaks off, exposing the underlying Si to the electrolyte [43, 44]. So continuous formation/cracking of SEI is accompanied by loss of active Li and electrolyte, which eventually leads to capacity degradation [5]. One effective attempt to solve this issue is the introduction of electrolyte additives such as fluoroethylene carbonate (FEC) [45] and vinylene carbonate (VC) [46]. It has been reported that an optimized amount of these additives can modify the SEI to a thinner, less dense, or more flexible layer due to the increase of polymeric components, versus inorganic compounds, which can better withstand the mechanical strains of the Si-based anode, while providing a high Li ion diffusion path, increase the Coulombic efficiency and enhance the capacity retention [47–50].

While it is crucially important to test and optimize the performance of a Si-based anode in a half cell structure as described above, it is necessary to evaluate and optimize the performance of the anode when it is paired with a suitable cathode in a full-cell configuration. The proper assembly of such high-capacity anode materials in a balanced battery exploiting conventional cathodes remains a challenge. A correct anode to cathode balance (in terms of specific capacity and weight) is a key requirement [51] to assure proper battery performances in terms of cycle life and capacity stability. In fact, as discussed so far, most of the works in literature have only focused on investigating the electrochemical performance of Si-based anode in a half-cell pairing with a Li metal counter electrode that provides an unlimited source of Li [52, 53]. So even if the material shows a very good electrochemical behaviour in the half cell (e.g. 90% capacity retention after 5000 cycles at 6 A g^{-1} [54], >95% capacity retention after 2800 cycles at 1.4 A g^{-1} [55], or 80% capacity retention after 1000 cycles at 1 A g^{-1} [56]) it could not be necessarily operating well when it is matched with a Li metal oxide as the cathode in a real cell configuration. In addition to the mismatching of the capacities of anode and cathode, continuous growth of SEI, trapping Li ions in the matrix and SEI, and dissolution of the electrode materials are some of the issues in a full cell that might result in a low Coulombic efficiency and fast capacity decay of the battery [5, 57]. These issues explain the limited number of reports on silicon-based full cells. Some of the recent works on developing a full cell based on a Si-based anode and different types of cathode are summarized in table 1. Most of these full cell performances, show a limited cyclic stability (<100 cycles) and low capacity retention, which is not validated for the real-world applications [4, 34, 58–64].

Motivated by the above considerations, here in this work, we report a full-cell Li-ion battery, in which a Si-based anode matches with a commercial NMC_{111} cathode. We show that after proper optimization, the full cell can deliver an areal capacity >1.6 mAh cm^{-2} with a capacity retention >90% after

300 cycles when cycled at C/2. In order to develop the Si/G/C nanocomposite, a scalable WJM process was used [32], followed by a glucose-assisted modification step to create a thin layer of carbon coating on the surface of Si nanoparticles (NPs). The electrode was first evaluated in the half-cell showing an excellent cyclic stability and rate capability owing to the homogenous distribution of Si NPs in the conductive graphene network and the ability of the electrode to maintain its structure upon cycling and then used in the full-cell following pre-lithiation to compensate for the Li ions trapped in the structure during the first lithiation cycle. The comparison between Si/G and Si/G/C full cells clearly shows the positive role of the glucose-derived carbon coating on both the electrochemical stability and mechanical integrity of the electrode by preventing the detachment of Si NPs from the graphene matrix and the direct contact of the electrolyte with Si NPs, thus further stabilizing the SEI [65].

2. Experimental section

2.1. Materials

Silicon NPs (<100 nm diameter) and graphite flakes (+100 mesh) were purchased from Sigma-Aldrich and D-(+)-Glucose, anhydrous, 99% was purchased from Alfa Aesar.

2.2. Preparation of Si/graphene (Si/G) nanocomposite by WJM

Si/G powder was prepared by WJM process developed in our group [32] according to the following process. In a typical process, 5 g of graphite powder and 5 g of spherical Si NPs (Si NPs) were dispersed in 1 l of *N*-methyl-2-pyrrolidone (NMP) (>97%, Sigma Aldrich) by mechanical stirring. The dispersion was pushed through a set of perforated interconnected disks (processors) by a hydraulic mechanism and a piston applying a pressure of 180–250 MPa [32]. Two jet streams were generated at the second disk containing two holes with diameters of 1 mm [32]. Next, the jet streams went between the second and the third disk, which consists of a nozzle with a diameter of 0.3 mm [32]. Exfoliation of graphite was promoted by the shear force generated while the solvent passes the nozzle [32]. Then the sample was divided into two streams which was recombined in the last disk before leaving the processor and a chiller was used to cool down the sample [32]. The WJM process was repeated by passing the sample through the 0.20, 0.15 and then 0.10 mm nozzles. The full characterization of the FLG flakes is reported in our previous work [32]. Finally, the sample was collected and the NMP was evaporated and exchanged to ethanol using a rotary evaporator [66]. The obtained powder, labelled as Si/G, was then dried in the vacuum oven at 60 °C to completely remove the solvent overnight.

2.3. Preparation of Si/G/C nanocomposite

The as-prepared powder in the previous step was mixed with glucose powder in the weight ratio of 1–1 (Si/G to glucose) using a mortar and pestle and heat-treated at 750 °C 30 min in a tube furnace to carbonize the glucose under Ar atmosphere plus 5 sccm H_2. The sample was first heated to 700 °C with a heating rate of 15 C min^{-1} and then 10 C min^{-1} to 750 °C for 30 min. The obtained powder was labelled as Si/G/C. Figure 1 shows the schematic illustration of the synthesizing route.

2.4. Materials characterization

The morphology of Si/G and Si/G/C samples was studied by scanning electron microscopy (SEM) by a JEOL JSM-6490LA instrument, unless otherwise specified. Bright-field transmission electron microscopy (BF-TEM) images were acquired on a JEOL JEM-1400Plus microscope (LaB_6 source), operated at 120 kV. High-resolution TEM (HRTEM) and energy-filtered TEM (EFTEM) images were acquired on an image-Cs-corrected JEOL JEM-2200FS microscope, equipped with an in-column energy filter (Ω-type). The EFTEM elemental maps presented here, obtained by the three-window method, were acquired at the K ionization edge of carbon (16 eV slit width) and oxygen (30 eV slit width) and at the L_{23} ionization edge of silicon (10 eV slit width). For TEM analyses, the samples (powders and fragments of electrodes) were suspended in toluene and sonicated, and a small volume of suspension was drop-cast onto holey-carbon-coated Cu grids. Powder x-ray diffraction (XRD) (PANalytical Empyrean x-ray diffractometer equipped with a 1.8 kW Cu Kα ceramic x-ray tube) and x-ray photoelectron spectroscopy (XPS) (Kratos Axis UltraDLD spectrometer, using a monochromatic Al Kα source operated at 15 kV and 20 mA) were employed to investigate the crystal structure and surface chemistry of the materials, respectively. Thermo-gravimetric analysis (TGA) was conducted (TGA Q500-TA Instrument) in air over a temperature range of room temperature to 900 °C at a heating rate of 5 °C min^{-1}. Raman measurements were carried out using a Renishaw inVia spectrometer using a 50× objective (numerical aperture 0.75), and a laser with an excitation wavelength of 514.5 nm with an incident power of B5 mW. The Si/G and Si/G/C powder were dispersed in NMP and drop casted onto a Si wafer (LDB Technologies Ltd) covered with 300 nm thermally grown SiO_2.

2.5. Electrochemical measurements

The electrochemical performance of the pristine Si, Si/G and Si/G/C samples was evaluated using CR2032 coin cells. The electrodes were prepared by mixing the Si/G or Si/G/C powders with conductive carbon black (super P) and binder (PAA/CMC (1/1)) dissolved in deionised water in the weight ratio of 80:10:10. The slurry was then coated onto the copper foil, dried

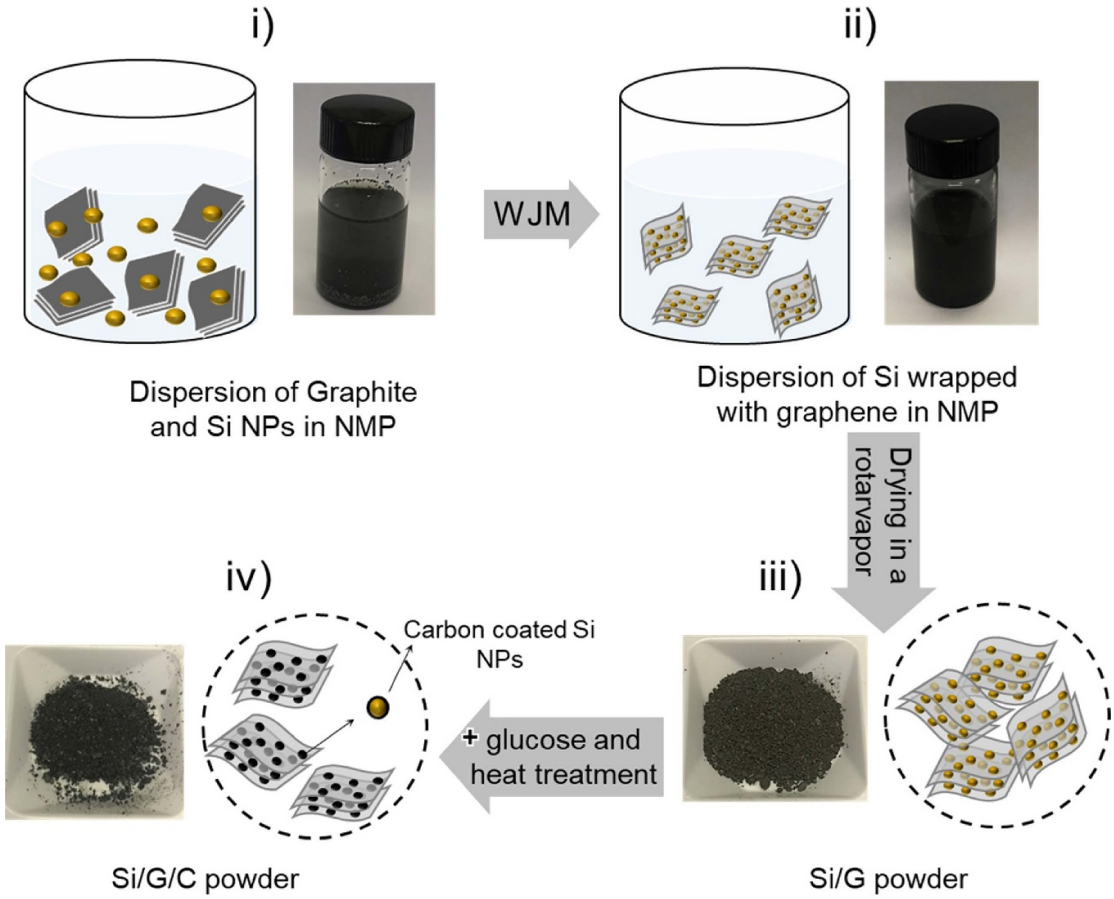

Figure 1. Schematic illustration of the synthesizing process; (i) dispersing graphite and silicon nanoparticles in NMP, (ii) dispersion of silicon wrapped with FLG in NMP after wet-jet milling, (iii) silicon/graphene powder after solvent evaporation in a rotary evaporator, (iv) mixing with glucose and annealing to obtain silicon/graphene/carbon powder.

under vacuum at 150 °C overnight. Disks of 10 mm in diameter with a film density of ~1.09 g cm^{-3} were cut and used as working electrodes in coin cells. The cells were assembled in an Ar-filled glovebox with a Li foil as the counter electrode. The electrolyte consisted of LP30 (solvionic) (1 M $LiPF_6$ in dimethyl carbonate (DMC):ethylene carbonate (EC) = 1:1 v/v) and 5 wt.% of FEC as additives embedded in a Whatman borosilicate separator. The coin cells were tested on a Biologic battery tester at different current densities between 0.1 and 1 V. The cyclic voltammetry (CV) test was also performed with a scan rate of 0.2 mV s^{-1}. The mass loading of Si was taken into account to calculate the capacities. Here we mainly focus on the role of the additional carbon coating (comparison between Si/G and Si/G/C) and the full cell behaviour. Additional characterization of the Si/G composite as anode in Li-ion half cells has been reported in our previous work [67].

3. Results and discussion

3.1. Materials characterization

The XRD patterns of the pristine Si, Si/G and Si/G/C samples are shown in figure 2(a). Sharp characteristic peaks of Si are clearly observed in the 2θ range of 20–90° located at 28.27, 47.27, 56.08, 69.08, 76.32 and 87.96 corresponding to the (111), (220), (311), (400), (331) and (422) reflections well-fitted with the cubic (Fd-3m) Si [68, 69]. The other peaks show the characteristics of graphite with the main peak located at 26.5° corresponding to (002) reflection [34, 70]. Figures 2(b) and S1 (available online at stacks.iop.org/2DM/8/035014/mmedia) show the SEM images of the Si/G/C and Si/G nanocomposites, respectively. In the lower magnification (figures 2(b) and S1(a)), FLGs are seen to create an interconnected conductive and porous network, which can facilitate the ion diffusion and electron transfer within the sample [33, 34]. The inset of figure 2(b) shows the higher magnification of the rectangular area marked in figure 2(b) showing the uniform dispersion of Si NPs in between FLG flakes as in figure S1(b). Elemental maps energy-dispersive X-ray spectroscopy (EDS) and analysis of the Si/G/C sample is presented in figure S2 confirming the uniform dispersion of C and Si elements in the sample. The oxygen peak is also detected in the chemical analysis due to the surface oxidation of the Si NPs.

TEM analyses of the Si/G and Si/G/C sample are presented in figure 3. Spherical Si NPs are seen in figure 3(a) dispersed within a graphene flake in Si/G sample. Figures 3(b) and (c) (the rectangular

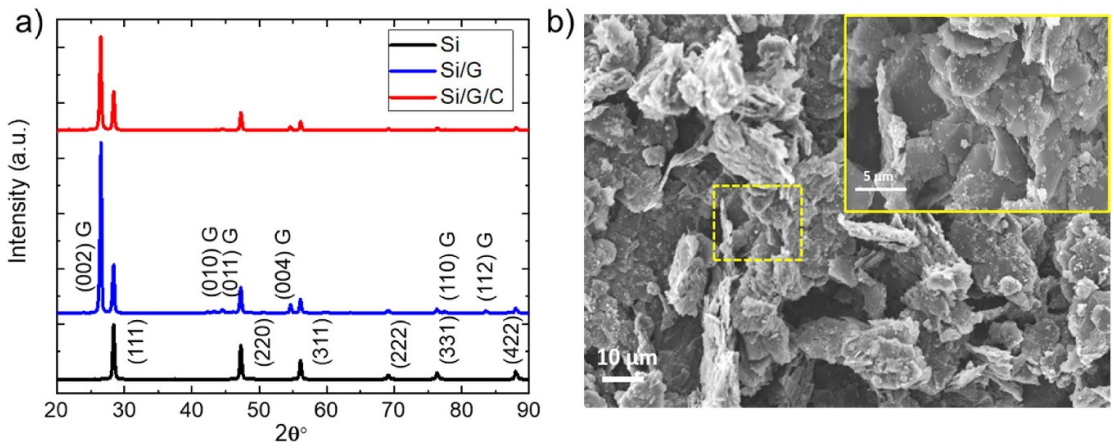

Figure 2. (a) XRD patterns of Si, Si/G and Si/G/C; (b) low magnification and (inset of b) high magnification SEM image of Si/G/C nanocomposite.

area in figure 3(b)) show the nanostructure of the sample after mixing with glucose and carbonization heat treatment (Si/G/C). It can be observed that the Si NPs are still nicely dispersed within the FLG matrix. Besides, a thin carbon coating layer with the thickness of <10 nm is observed covering the Si NPs. This surface coating that can cover the whole structure (both on FLG flakes and Si NPs) comes from the decomposition of glucose at high temperatures (200 °C–500 °C) under Ar [71–73], and it has an important effect on the electrochemical performance, since it can prevent the detachment of the Si NPs from FLG flakes [74, 75]. HRTEM analysis of Si nanoparticle (figure 3(d)) confirms its crystalline nature [76, 77]. Elemental mapping of an individual Si NP by EFTEM for Si, C and O are presented in figures 3(f)–(h). Existence of O reveals the surface oxidation of Si NPs, which is very common [34, 78, 79], and the existence of C again confirms the formation of thin amorphous carbon layer on the surface of NPs. Additional HRTEM image of an individual Si NP in Si/G/C sample has been provided in figure S3 along with its fast Fourier transform (FFT) analysis further confirming the crystalline nature of the Si NPs that are in contact with FLG flakes (figure S3(c)).

In order to quantify the Si to C ratio in the samples, TGA was performed in air for Si, Si/G and Si/G/C materials, and the resulting curves are plotted in figures 4(a) and S4. For Si/G and Si/G/C samples, the weight loss below 220 °C is due to the loss of moisture, which is followed by a sharp weight loss at ~690 °C due to the burning of graphene. There is a second weight loss at ~490 °C for Si/G/C sample corresponding to the burning of carbonized glucose, which is consistent with the existence of the carbon coating [80, 81]. Since Si is oxidized in air at higher temperatures, TGA was also carried out on pristine Si powder to accurately quantify the increase of mass. Considering the above explanations, the mass of Si is calculated as ~50 wt% and ~32 wt% in Si/G and Si/G/C samples, respectively.

The general and deconvoluted XPS spectra of Si 2p and C 1s elements for Si/G/C are shown in figures 4(b)–(d). The Si 2p spectrum (figure 4(c)) exhibited four peaks centred at 98.8, 99.5, 100.1 and 103.25 eV, corresponding to Si $2p_{3/2}$, Si $2p_{1/2}$, SiO_{x-y} and SiO_x, respectively [82–85], confirming the presence of an oxide layer. The C 1s spectrum (figure 4(d)) shows four peaks, including sp^2 and sp^3 carbon bonds at 284.2 and 284.7 eV, C–O at 285.3 eV and O–C=O at 289.4 eV [86–88]. The latter two peaks originate from the carbon bonds in the functional groups of the amorphous carbon coming from the decomposition of glucose [86].

Raman spectroscopy is a powerful tool to investigate the graphitization degree and the defect density [89] of C-based (nano)materials [90] and hybrid (nano)structures [91]. The Raman spectra of Si/G and Si/G/C are compared in figure S5 showing an intense peak of crystalline Si at ~518 cm^{-1} assigned to the optical phonons and a less-intense peak at ~956 cm^{-1} attributed to the overtones of optical phonons [92, 93]. In a typical Raman spectrum of amorphous carbon/graphite/graphene, the G and D peak are, respectively positioned at ~1585 cm^{-1} and 1350 cm^{-1} [90]. The G peak corresponds to the E_{2g} phonon at the Brillouin zone center [90], while the D peak is due to the breathing modes of the sp^2 rings and requires a defect for its activation by double resonance [90]. The 2D peak at ~2680 cm^{-1} is the second order of the D peak but defects are not required for their activation [90]. The width and intensity of D and G peak (Si/G/C:I_D/I_G = 0.78, Si/G:I_D/I_G = 0.2) indicates the presence of amorphous carbon in Si/G/C sample [94, 95], confirming the TEM data discussed previously.

3.2. Electrochemical characterization

The electrochemical performance of the Si/G/C nanocomposite is presented in figure 5. The CV curves of the Si/G/C electrode obtained in the first five cycles are plotted in figure 5(a). Upon the first

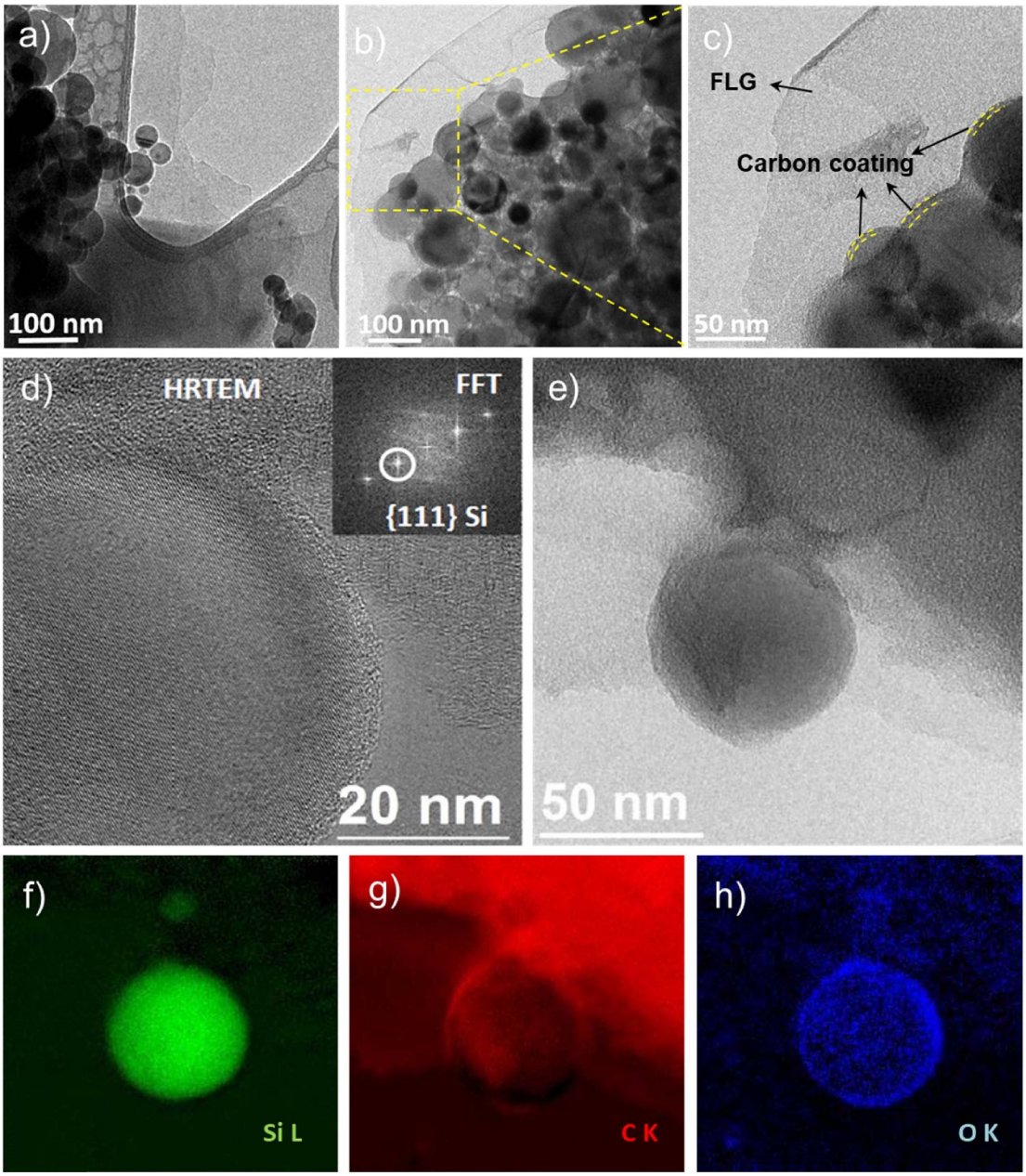

Figure 3. (a)–(c) BF-TEM images of (a) Si/G and (b), (c) Si/G/C. (d) HRTEM image of an individual Si NP in the sample Si/G/C, with (inset) its fast Fourier transform showing the {111} planes of cubic Si (ICSD 51 688). (e) Elastically-filtered (zero-loss) TEM image of an individual NP in samples Si/G/C and (f)–(h) corresponding EFTEM elemental maps for (f) Si, (g) C and (h) O.

discharge (lithiation) process, starting from the open circuit potential (typically between 2.5–3 V) to 0.01 V the following reactions take place; (a) electrolyte decomposes in two steps, first FEC at ∼1.15 V and then EC and DMC at lower potential (∼0.8 V) forming a SEI on the surface of the electrode [23, 96, 97]. These reactions can be correlated with the sloping plateau of the 1st discharge curve in figure 5(b), which disappear in the following cycles; (b) reduction of native oxide layer (SiO_x) of crystalline Si NPs at ∼0.43 V [98], and (c) the reaction of Li with crystalline Si through an alloying process at potentials <0.28 V [98, 99]. Based on the equilibrium phase diagram, Si should react with Li in different steps, which intermediate Li–Si phases form at distinct potentials. However, this only happens at high temperature [100]. At room temperature, the reaction (equation (1)) will appear in the charge/discharge profiles with a flat plateau, as can be seen in the 1st discharge curve in figure 5(b) [100, 101]. In the following discharge cycles, the reaction of Li with Si shifts to higher potential (∼0.2 V). Upon charging, delithiation (de-alloying) of the Si occurs at 0.3 and 0.5 V [98, 99, 102]. This is accompanied with the transformation from crystalline to amorphous state of Si, which happens in two steps. It should be noted that the peaks at lower potentials (below 0.1 V) during the 1st charge and discharge process, are correlated to the intercalation of Li ions in between FLG flakes. After the formation cycle, the potential window is

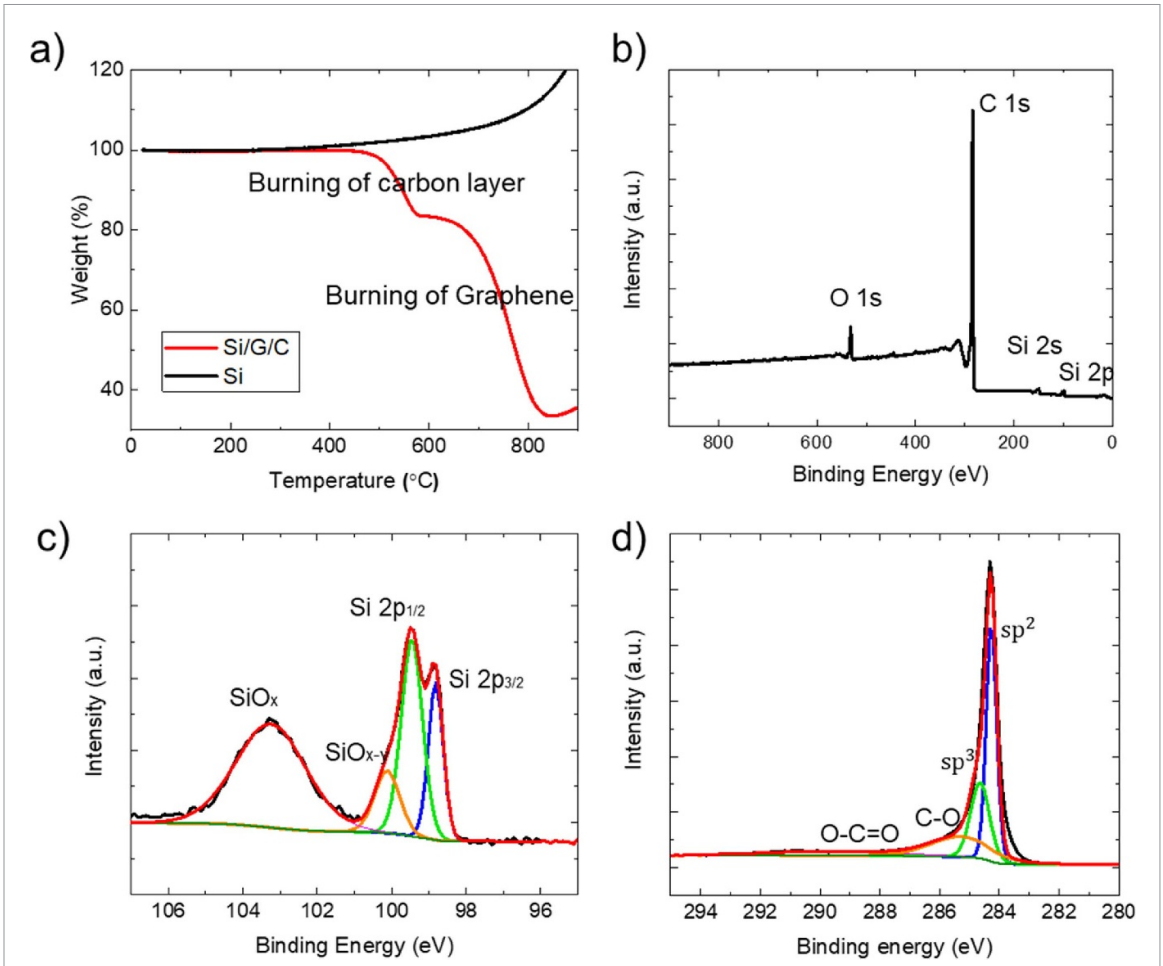

Figure 4. (a) TGA of Si and Si/G/C samples, (b)–(d) general and deconvoluted XPS spectra of Si/G/C sample.

limited to 0.1–1 V to eliminate the contribution of FLG and so these peaks disappear afterwards. The overlap of the CV curves from 2nd to 5th cycle, indicates the stability in the electrochemical behaviour of the Si/G/C electrode in terms of capacity and the reactions reversibility [89, 103].

The cyclic performance of the Si/G/C electrode is presented in figure 5(c). This can be compared with the cyclic performance of Si/G electrode in figure S6, showing much more stability of the Si/G/C over Si/G electrode with a capacity retention of ∼91% and 68.5% at 100th cycle, respectively, and the important role of the carbon coating for the electrochemical stability. The thin layer of carbon coating improves the contact of the Si NPs to the FLG flakes and can prevent the detachment of NPs from the FLG flakes upon charge/discharge cycles [75, 104]. The Coulombic efficiency of the first cycle is as high as 80.3% and it is fully recovered to >98% at the 5th cycle and afterward. The specific capacity of the electrode reaches ∼1770 mAh g^{-1} after 200 cycles at 200 mA g^{-1} (0.05 C) with a capacity retention of ∼80% and a capacity fading rate of 0.09% per cycle. The capacity retention of the Si/G/C electrode is significantly higher than the one of both pristine Si (∼14.5% after 100 cycles) and Si/G electrode (68.5% after 100 cycles) (figure S6(a) and (b)).

The electrochemical performance of the Si/G/C electrode has been tested at higher current densities (i.e. >0.2 A g^{-1}) and the result is shown in figure 5(d). The nanocomposite shows a gradual capacity loss with the increase of the current density. However, it can still deliver a high capacity of >875 mAh g^{-1} at a high current density of 6 A g^{-1}. By decreasing the capacity to the first step (200 mAh g^{-1}), electrode can recover all of its capacity and shows almost the same value of the initial stage. The rate capability of the Si/G electrodes are also tested and shown in figure S6(c). In all of the current densities, the specific capacity of Si/G electrode is lower than Si/G/C electrode. These results again show the excellent stability (>80% capacity retention after 200 cycles) of the Si/G/C nanocomposite and the key role of graphene and carbon layer to provide efficient electron and ion pathways during charge/discharge cycles.

Post-mortem analysis was carried out to further investigate the structural changes of the Si/G/C electrodes over cycling. Top and cross-section view of the as-prepared Si/G/C electrode and the electrodes after 100 cycles are shown in figures 6(a)–(d). The

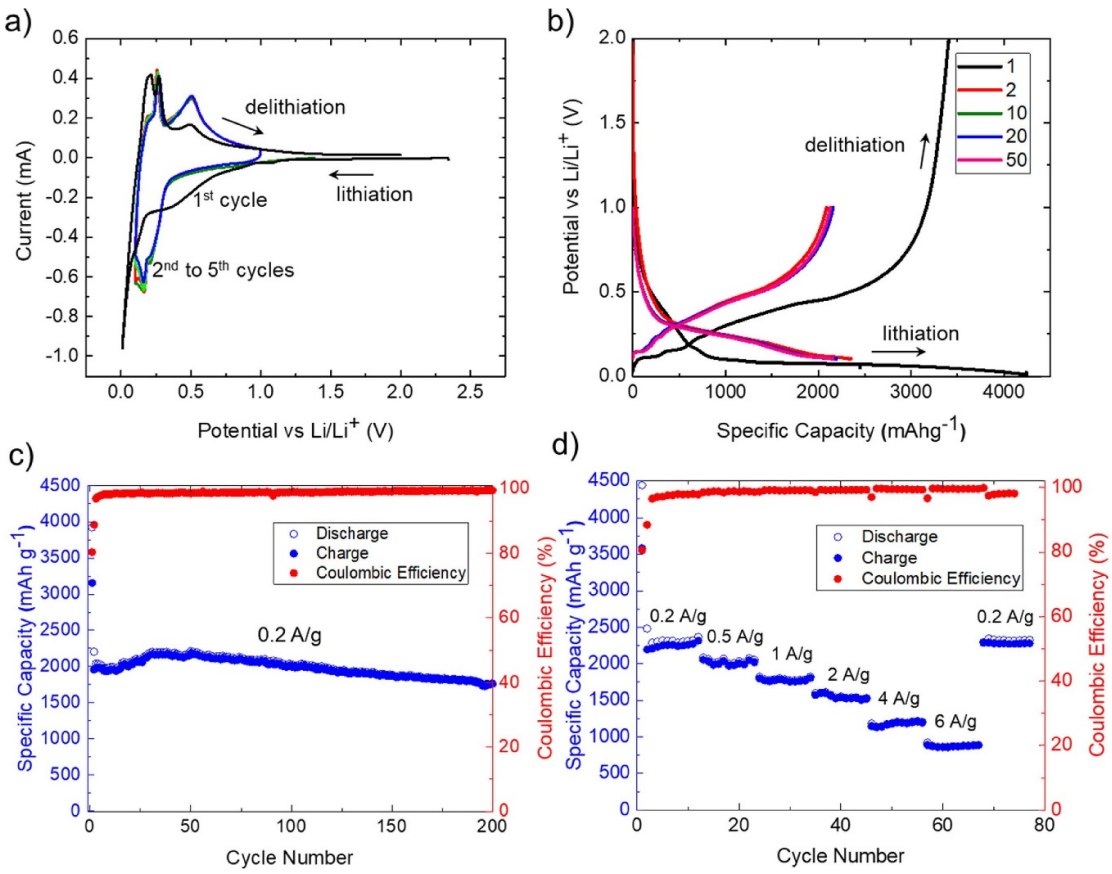

Figure 5. (a) CV curves; (b) charge/discharge profiles; (c) cyclic performance and (d) rate performance of Si/G/C electrodes.

as-prepared electrode exhibits a fine dispersion of Si, graphene, super P and the binder. Of particular interest is the porous layered structure of the electrode, see cross-section view of figure 6(b), which increases the electrode-electrolyte interactions for electrochemical reactions and facilitates the ion and charge transfer processes. Investigating the structure of the electrode after 100 charge/discharge cycles, figures 6(c)–(i) show that side-products have been formed on the surface of the electrode. However, the porous structure of the electrode is maintained and the FLG flakes can still be recognized. The HRTEM images in figure 6(f) confirms that the Si has completely transformed into an amorphous state after cycling, while from the elemental maps (figures 6(g)–(i)) O and C are present on the surface of the Si clusters.

In order to show the real application of our Si/G/C nanocomposite in full cell configuration, we coupled it with NMC_{111} as cathode (see the scheme in figure 7(a)). The mass ratio of the cathode and anode was balanced according to their performances in half cell configuration. The so-called negative to positive (N/P) electrode capacity ratio was maintained at 1.1–1.2 using the appropriate mass loadings of anode and cathode. Figure S7 shows the half-cell performance of the balanced NMC_{111} and Si/G/C electrodes. Figure 7(b) shows the areal capacity of the full cell versus the cycle number. The battery was cycled under C/20 in the first charge/discharge cycle and then the current increased to C/2 in the following cycles. The full cell exhibits an areal capacity of 2.24 and 1.57 mAh cm^{-2} in the first charge and discharge cycle, respectively, resulting in an initial Coulombic efficiency of ~70%. The Coulombic efficiency rises to 94.5% and then 98% in the following cycles. For comparison, the full cell of Si/G electrode versus NMC_{111} was tested under the same condition. The better cyclic stability of the Si/G/C-NMC_{111} battery, compared to Si/G-NMC_{111} one, can be attributed to the existence of the carbon layer, which can retain the nanostructure of the electrode over charge/discharge cycles.

It should be noted that an excellent cyclic stability (i.e. a capacity retention of >80%) and a high first cycle Coulombic efficiency are two key figures of merit for an ideal full cell. The reason for the relative low initial Coulombic efficiency of the full cell reported above compared to the commercial Li ion batteries using graphite as anode (>85%) [105], is originating from the trapping of Li ions in the matrix and SEI layer during the first lithiation [105, 106]. An efficient strategy to improve the initial Coulombic efficiency is to pre-lithiate the anode by inserting excess Li in the structure [107, 108]. Besides improving the initial Coulombic efficiency, it has been also shown that a pre-lithiated Si-based anode has a higher

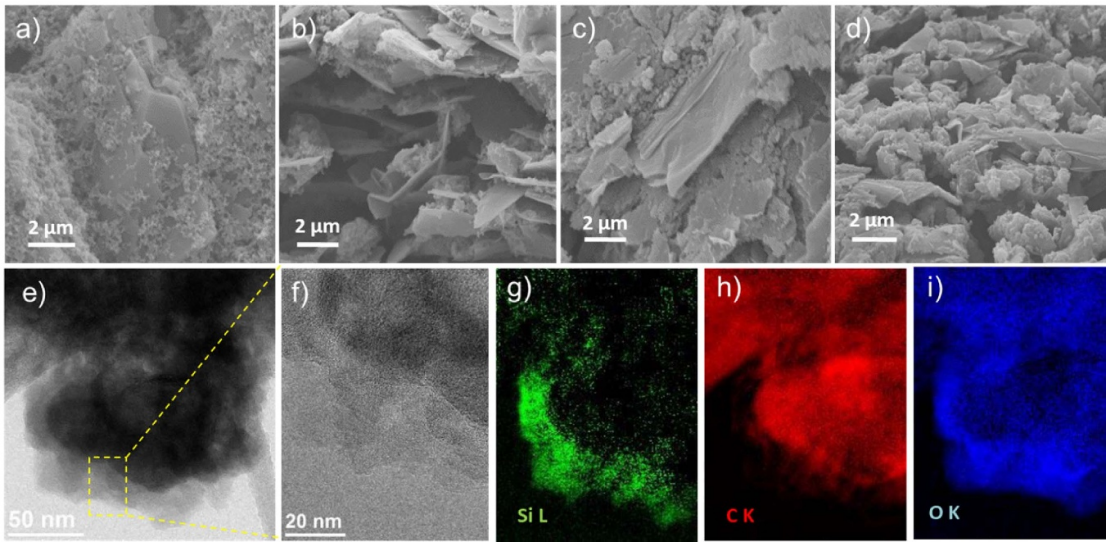

Figure 6. SEM images of top view (a) and cross-section view (b) of fresh Si/G/C electrode; (c), (d) SEM images of top view (c) and cross-section view (d) of Si/G/C electrode after 100 cycles. (e) Elastically filtered (zero-loss) TEM image of a region partly suspended on a hole in the carbon support film; (f) HRTEM image of a region in (e), showing the amorphous structure of Si and corresponding EFTEM elemental map for (g) Si, (h) C and (i) O for Si/G/C electrode after 100 cycles (g)–(i).

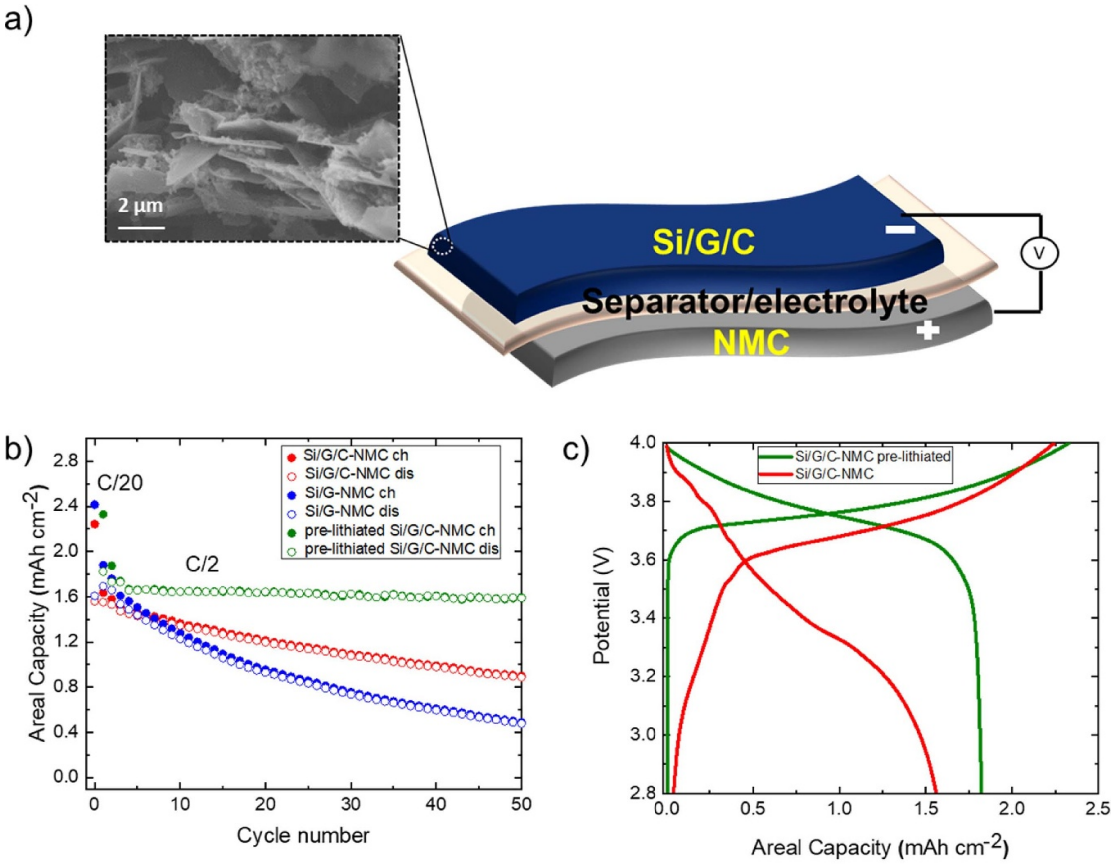

Figure 7. (a) Schematic of the full cell configuration, (b) cyclic performance of full cells with Si/G, Si/G/C and pre-lithiated Si/G/C as anodes vs NMC_{111}, (c) comparing 1st charge/discharge profiles of Si/G/C and pre-lithiated Si/G/C electrode.

Li ion diffusion coefficient [107], which boosts the reaction kinetics [107, 109] and reduce the mechanical strains generated during alloying/de-alloying process [107]. Consequently, the pre-lithiation prevents the deterioration of the structure and improves the stability of the cell over cycling [107, 108]. Different techniques have been reported to pre-lithiate the Si electrode including the electrochemical way, using stabilized Li metal powder (SLMP) [61] or a self-discharge mechanism [110]. Here in this work,

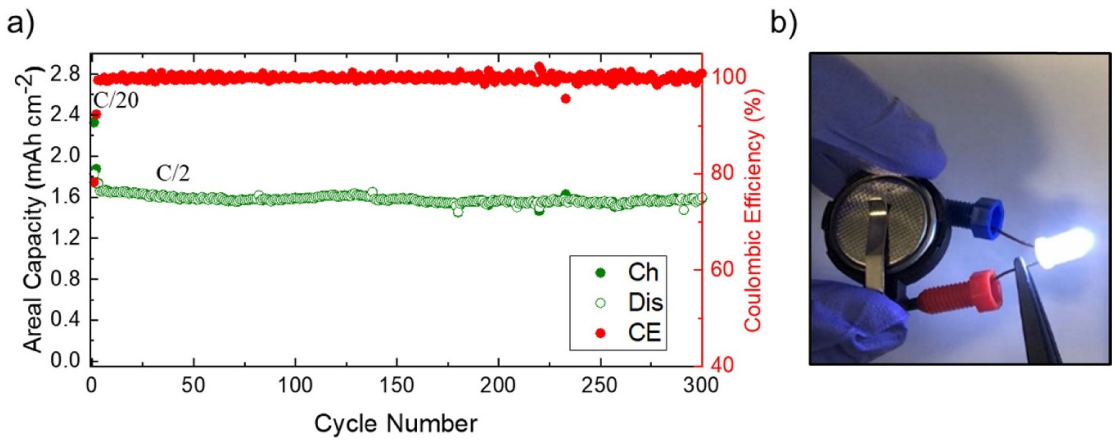

Figure 8. (a) Long cycle performance of pre-lithiated Si/G/C-NMC full cell, (b) photograph of the full cell lighting up a light emitting diode (LED).

Table 1. Comparison of the electrochemical performance of different Si-based Li-ion full-cells.

Anode	Cathode	Electrolyte	Current density	Capacity retention (%)	Ref
Graphene/Si multilayer	NMC_{111}	1 M $LiPF_6$	C/4	70.4% after 15 cycles	[52]
Si/Gr/CNM	NCA	1 M $LiPF_6$	C/2	75% after 100 cycles	[112]
Si/Graphite/ Graphene	LFP	1 M $LiPF_6$	C/2	60% after 50 cycles	[59]
Si-kerf	NMC_{442}	1 M $LiPF_6$ + 15 V% FEC	C/2	42% after 100 cycles	[113]
Micro Si/r-GO/CNT	NMC_{111}	1 M $LiPF_6$ + 1 wt% VC	C/10 then C/3	65.5% after 50 cycles	[60]
Si/Graphite	NMC_{111}	1 M $LiPF_6$ + 10% FEC	—	63% after 50 cycles	[4]
Si/CNT	NCA	1.2 M $LiPF_6$	C/10 then C/5	92% after 50 cycles	[58]
SiO	NMC_{111}	1 M $LiPF_6$ + 30 wt% FEC	—	76.6% after 140 cycle	[114]
SiO_x	NCA	1 M $LiPF_6$ + 5 wt% FEC	C/20 then 1 C	75.8% after 100 cycles	[105]
Si-PEG-G	LCO	1 M $LiPF_6$ + 5 wt% FEC	C/10 then 1 C	89% after 80 cycles	[61]
Si-graphene	NCA	1 M $LiPF_6$	C/15 then C/5 then C/2	82.9 5 after 50 cycles	[62]
Al_2O_3/Si/ graphene	$Li_{1.2}Ni_{0.2}Mn_{0.6}O_2$	1 M $LiPF_6$	C/5	65% after 100 cycles	[115]
gSi/C	LCO	1 M $LiPF_6$	C/10 then C/2	73.3% after 50 cycles	[63]
Si/C spheres	LCO	1 M $LiPF_6$	C/2	62.5 after 100 cycles	[64]
Si/FLG/C	NMC_{111}	1 M $LiPF_6$ + 10 V% FEC	C/20 then C/2	82% after 20 cycles	[34]
Si/Graphene	$LiMn_2O_4$	1 M $LiPF_6$	0.4 mA	71% after 30 cycles	[116]
Si/G/C	NMC_{111}	1 M $LiPF_6$ + 5 wt% FEC	1st at C/20, then C/2	91% after 300 cycles	This work

pre-lithiation was carried out through the direct contact of Li foil and Si/G/C electrode in the presence of the electrolyte [109, 111]. Pressure was applied using two pieces of glasses and clips for 12 h. The electrode was then washed with DMC and used directly to assemble the full cell with NMC_{111}. The cyclic performance of the pre-lithiated cell is compared with the non-pre-lithiated cell, see figure 7(b), showing a much better initial Coulombic efficiency of ~80% and capacity retention of 91% after 50 cycles at C/2. The pre-lithiated cell was also tested at higher current densities up to 5 C and the result is presented in figure S9. The full cell can still deliver an areal capacity of >1.3 and 0.8 mAh cm^{-2} at high currents of 1 C and 2 C, respectively. The capacity decreases significantly at 5 C. However, by decreasing the current density to C/2, the areal capacity has been recovered.

The first cycle charge/discharge profile of the pre-lithiated cell is presented in figure 7(c) and

compared with the cell without pre-lithiation. It is interesting to note that the working voltage of the pre-lithiated cell is ∼3.7 V versus ∼3.4 V for the other cell. The gravimetric energy density of the two cells were calculated by integrating the area under the first discharge curve considering the total mass of the anode and cathode active materials. The energy density is calculated as ∼325 Wh kg^{-1} for the Si/G/C-NMC_{111} cell and ∼395 Wh kg^{-1} for the same cell with pre-lithiation. To demonstrate how the developed Si-based electrode can be compared to a conventional graphite anode, electrodes with similar areal capacities made of Si/G/C and graphite have been compared and reported in figure S8. In the case of the Si/G/C electrode, the mass loading of the film was measured as 4.3 mg cm^{-2}, while this value is 7.5 mg cm^{-2} for the graphite electrode. This comparison shows that with similar areas of the electrodes, ∼43% less material is required for Si/G/C anode to reach the same areal capacity of the graphite-based one. This result can be translated to a higher gravimetric energy density (Wh kg^{-1}) of the cell based on Si/G/C anode compared to the graphite one.

The long cycle test of the pre-lithiated cell is demonstrated in figure 8(a), showing a capacity retention of 91% after 300 cycles at C/2. Figure 8(b) shows the photograph of the working cell able to power a light emitting diode (LED).

Table 1 summarizes the electrochemical performances of different Si-based full cells reported in literature and compared with the one developed in this work. It should be noted that the cyclic stability of the full cell developed in this work is among the highest values reported so far, further confirming the high potential of the material in real applications.

4. Conclusion

New scalable strategy has been proposed to prepare Si-graphene composites (Si/G), which can be exploited as anode in high energy density Li-ion batteries. WJM process has been used to simultaneously exfoliate graphite flakes into FLG flakes and encapsulate Si NPs in between these flakes. An amorphous carbon coating was designed in order to further improve the mechanical integrity of the nanostructure, improving the electrical contacts of Si nanoparticle with the FLG matrix. The Si/G/C electrodes have been tested both in half-cell and full-cell configuration delivering an excellent electrochemical performances. The following points are highlighted from this work:

(a) Scalable WJM process was used to produce Si/G nanocomposite through a simultaneous exfoliation of graphite flakes and encapsulation of Si NPs in between the FLG flakes. The uniform dispersion and encapsulation of Si NPs is easily achievable through the WJM process. The process was followed by mixing Si/G and glucose as a second carbon source and a heat treatment process under controlled atmosphere, creating a thin amorphous carbon coating on the surface of the Si NPs. The porous structure of the nanocomposite provides active sites for electrochemical reactions, while it can buffer the volume expansion of the Si NPs upon lithiation, preventing re-agglomeration of particles. Besides, the thin carbon layer (<10 nm) acts as a glue to keep the particles attached to the conductive FLG matrix, improving the electron transfer processes and maintaining the integrity of the nanostructure.

(b) The Si/G/C electrode has shown a capacity of ∼1770 mAh g^{-1} after 200 cycles at 0.2 A g^{-1} corresponding to a capacity retention of 80%. The electrode can still deliver a capacity >875 mAh g^{-1} at a high current density of 6 A g^{-1}. Overall the Si/G/C electrode has shown better performance compared to the pristine Si and Si/G electrodes tested in the same conditions. This observation is attributed to the unique nanostructure of the electrode described above.

(c) The Si/G/C electrode was tested in a full-cell configuration matched with a NMC_{111} cathode. The full-cell, with a pre-lithiated anode, has shown a remarkable initial Coulombic efficiency of ∼80% and a superior capacity retention of 91% after 300 cycles at C/2. The energy density of the full-cell was calculated as ∼395 Wh kg^{-1}.

(d) The electrochemical performance of the Si-based anodes reported in this study, coupled with the scalable synthesis method, shows remarkable potential to design high energy density Li-ion batteries that can compete with the commercial ones based on graphite anodes.

Acknowledgments

We thank Doriana Debellis and Luca Leoncino from the Electron Microscopy Facility at the Fondazione Istituto Italiano di Tecnologia for help with SEM and TEM characterization and Christoph Stangl of Varta Micro Innovation gmbH for providing cathode material.

Conflict of interest

The authors declare no competing financial interest.

Funding Sources

We acknowledge the European Union's Horizon 2020 research and innovation program under Grant Agreement No. 785219, GrapheneCore2.

ORCID iD

Francesco Bonaccorso https://orcid.org/0000-0001-7238-9420

References

[1] Armand M and Tarascon J M 2001 *Nature* **414** 359–67
[2] Lin Z, Liu T, Ai X and Liang C 2018 *Nat. Commun.* **9** 8–12
[3] Pellegrini V, Bodoardo S, Brandell D and Edström K 2019 Challenges and perspectives for new material solutions in batteries *Solid State Commun.* **303–4** 113733
[4] Yim C H, Niketic S, Salem N, Naboka O and Abu-Lebdeh Y 2017 *J. Electrochem. Soc.* **164** A6294–302
[5] Jin Y, Zhu B, Lu Z, Liu N and Zhu J 2017 *Adv. Energy Mater.* **7** 1–17
[6] Franco Gonzalez A, Yang N H and Liu R S 2017 *J. Phys. Chem.* C **121** 27775–87
[7] Tao W, Wang P, You Y, Park K, Wang C Y, Li Y K, Cao F F and Xin S 2019 *Nano Res.* **12** 1739–49
[8] Pomerantseva E, Bonaccorso F, Feng X, Cui Y and Gogotsi Y 2019 *Science* **366** 6468
[9] Su X, Wu Q, Li J, Xiao X, Lott A, Lu W, Sheldon B W and Wu J 2014 *Adv. Energy Mater.* **4** 1–23
[10] Rahman M A, Song G, Bhatt A I, Wong Y C and Wen C 2016 *Adv. Funct. Mater.* **26** 647–78
[11] Andersson R, Hernández G, Edström K and Mindemark J 2020 *Energy Technol.* **8** 2000056
[12] Dou F, Shi L, Chen G and Zhang D 2019 *Electrochem. Energy Rev.* **2** 149–98
[13] Shen T, Yao Z, Xia X, Wang X, Gu C and Tu J 2018 *Adv. Eng. Mater.* **20** 1–15
[14] Zheng Y, Seifert H J, Shi H, Zhang Y, Kübel C and Pfleging W 2019 *Electrochim. Acta* **317** 502–8
[15] Chae S, Choi S-H, Kim N, Sung J and Cho J 2019 Integration of Graphite and Silicon Anodes for the Commercialization of High-Energy Lithium-Ion Batteries *Angew. Chem., Int. Ed.* **59** 110–35
[16] Zhang W, Zuo P, Chen C, Ma Y, Cheng X, Du C, Gao Y and Yin G 2016 *J. Power Sources* **312** 216–22
[17] Li P, Hwang J and Sun Y 2019 *ACS Nano* **13** 2624–33
[18] Aghajamali M, Xie H, Javadi M, Kalisvaart W P, Buriak J M and Veinot J G C 2018 *Chem. Mater.* **30** 7782–92
[19] Luo B and Zhi L 2015 *Energy Environ. Sci.* **8** 456–77
[20] Ho D N, Yildiz O, Bradford P, Zhu Y and Fedkiw P S 2018 *J. Appl. Electrochem.* **48** 127–33
[21] Nava G, Schwan J, Boebinger M G, McDowell M T and Mangolini L 2019 *Nano Lett.* **19** 7236–45
[22] Jia D and Huang J 2017 *New J. Chem.* **41** 4887–900
[23] Ashuri M and Shaw L L 2016 *Nanoscale* **8** 74–103
[24] Wu Z S, Zhou G, Yin L C, Ren W, Li F and Cheng H M 2012 *Nano Energy* **1** 107–31
[25] Hassoun J *et al* 2014 *Nano Lett.* **14** 4901–6
[26] Sun H *et al* 2016 *J. Mater. Chem.* A **4** 6886–95
[27] Papageorgiou D G, Kinloch I A and Young R J 2017 *Prog. Mater. Sci.* **90** 75–127
[28] Bonaccorso F, Colombo L, Yu G, Stoller M, Tozzini V, Ferrari A C, Ruoff R S and Pellegrini V 2015 *Science* **347** 6217
[29] Balandin A A 2011 *Nat. Mater.* **10** 569–81
[30] Pop E, Varshney V and Roy A K 2012 *MRS Bull.* **37** 1273–81
[31] Raccichini R, Varzi A, Passerini S and Scrosati B 2015 *Nat. Mater.* **14** 271–9
[32] Del Rio Castillo A E *et al* 2018 *Mater. Horiz.* **5** 890–904
[33] Greco E, Nava G, Fathi R, Fumagalli F, Del Rio-Castillo A E, Ansaldo A, Monaco S, Bonaccorso F, Pellegrini V and Di Fonzo F 2017 *J. Mater. Chem.* A **5** 19306–15
[34] Palumbo S, Silvestri L, Ansaldo A, Bonaccorso F and Pellegrini V 2019 *ACS Appl. Energy Mater.* **2** 1793–802
[35] Loveridge M J, Lain M J, Huang Q, Wan C, Roberts A J, Pappas G S and Bhagat R 2016 *Phys. Chem. Chem. Phys.* **18** 30677–85
[36] Magasinski A, Zdyrko B, Kovalenko I, Hertzberg B, Burtovyy R, Huebner C F, Fuller T F, Luzinov I and Yushin G 2010 *ACS Appl. Mater. Interfaces* **2** 3004–10
[37] Li C, Shi T, Yoshitake H and Wang H 2016 *J. Mater. Chem.* A **4** 16982–91
[38] Mazouzi D, Lestriez B, Roué L and Guyomard D 2009 *Electrochem. Solid-State Lett.* **12** 215–8
[39] Kuruba R, Datta M K, Damodaran K, Jampani P H, Gattu B, Patel P P, Shanthi P M, Damle S and Kumta P N 2015 *J. Power Sources* **298** 331–40
[40] Liu J, Zhang Q, Wu Z Y, Wu J H, Li J T, Huang L and Sun S G 2014 *Chem. Commun.* **50** 6386–9
[41] Karkar Z, Guyomard D, Roué L and Lestriez B 2017 *Electrochim. Acta* **258** 453–66
[42] Gu Y, Yang S, Zhu G, Yuan Y, Qu Q, Wang Y and Zheng H 2018 *Electrochim. Acta* **269** 405–14
[43] Jin Y *et al* 2017 *Energy Environ. Sci.* **10** 580–92
[44] Li Y, Yan K, Lee H-W, Lu Z, Liu N and Cui Y 2016 *Nat. Energy* **1** 15029
[45] Etacheri V, Haik O, Goffer Y, Roberts G A, Stefan I C, Fasching R and Aurbach D 2012 *Langmuir* **28** 965–76
[46] Qian Y, Schultz C, Niehoff P, Schwieters T, Nowak S, Schappacher F M and Winter M 2016 *J. Power Sources* **332** 60–71
[47] Wang J, Zhang L and Zhang H 2018 *Ionics* **24** 3691–8
[48] Rezqita A, Sauer M, Foelske A, Kronberger H and Trifonova A 2017 *Electrochim. Acta* **247** 600–9
[49] Jaumann T *et al* 2017 *Energy Storage Mater.* **6** 26–35
[50] Veith G M, Doucet M, Sacci R L, Vacaliuc B, Baldwin J K and Browning J F 2017 *Sci. Rep.* **7** 1–15
[51] Baasner A, Reuter F, Seidel M, Krause A, Erik P, Härtel P, Dör S, Abendroth T, Althues H and Kaskel S 2020 *J. Electrochem. Soc.* **167** 020516
[52] Ji L, Zheng H, Ismach A, Tan Z, Xun S, Lin E, Battaglia V, Srinivasan V and Zhang Y 2012 *Nano Energy* **1** 164–71
[53] Shobukawa H, Alvarado J, Yang Y and Meng Y S 2017 *J. Power Sources* **359** 173–81
[54] Wu H, Yu G, Pan L, Liu N, McDowell M T, Bao Z and Cui Y 2013 *Nat. Commun.* **4** 1943
[55] Zhu J, Wang T, Fan F, Mei L and Lu B 2016 *ACS Nano* **10** 8243–51
[56] Li X, Gu M, Hu S, Kennard R, Yan P, Chen X, Wang C, Sailor M J, Zhang J G and Liu J 2014 *Nat. Commun.* **5** 4105
[57] He Y, Xu G, Wang C, Xu L and Zhang K 2018 *Electrochim. Acta* **264** 173–82
[58] Forney M W, Ganter M J, Staub J W, Ridgley R D and Landi B J 2013 *Nano Lett.* **13** 4158–63
[59] Lin N, Xu T, Li T, Han Y and Qian Y 2017 *ACS Appl. Mater. Interfaces* **9** 39318–25
[60] Gao X, Wang F, Gollon S and Yuan C 2019 *J. Electrochem. Energy Convers. Storage* **16** 1–6
[61] Kim M K, Shin W H and Jeong H M 2019 *Appl. Surf. Sci.* **467–468** 926–31
[62] Eom K, Joshi T, Bordes A, Do I and Fuller T F 2014 *J. Power Sources* **249** 118–24
[63] Li C, Liu C, Wang W, Mutlu Z, Bell J, Ahmed K, Ye R, Ozkan M and Ozkan C S 2017 *Sci. Rep.* **7** 1–11
[64] Wang W, Favors Z, Li C, Liu C, Ye R, Fu C, Bozhilov K, Guo J, Ozkan M and Ozkan C S 2017 *Sci. Rep.* **7** 44838
[65] Zhang Y, Du N and Yang D 2019 *Nanoscale* **11** 19086–104
[66] Bellani S, Petroni E, Del Rio Castillo A E, Curreli N, Martín-García B, Oropesa-Nuñez R, Prato M and Bonaccorso F 2019 *Adv. Funct. Mater.* **29** 1–14
[67] Malik R *et al* 2020 *2D Mater.* **8** 015012

[68] Yang L Y, Li H Z, Liu J, Sun Z Q, Tang S S and Lei M 2015 *Sci. Rep.* **5** 10908
[69] Kim N, Oh C, Kim J, Kim J S, Jeong E D, Bae J S, Hong T E and Lee J K 2017 *J. Electrochem. Soc.* **164** A6075–83
[70] Chen X, Xiao T, Wang S, Li J, Xiang P, Jiang L and Tan X 2019 *Mater. Chem. Phys.* **222** 31–36
[71] Hou S C, Chen T Y, Wu Y H, Chen H Y, Lin X D, Chen Y Q, Huang J L and Chang C C 2018 *Sci. Rep.* **8** 1–11
[72] Ma F, Zhang X, He P, Zhang X, Wang P and Zhou H 2017 *J. Power Sources* **359** 408–14
[73] Li S R, Sun Y, Ge S Y, Qiao Y, Chen Y M, Lieberwirth I, Yu Y and Chen C H 2012 *Chem. Eng. J.* **192** 226–31
[74] Zhang B, Xu Z L and Kim J K 2014 *RSC Adv.* **4** 12298–301
[75] Fu K, Xue L, Yildiz O, Li S, Lee H, Li Y, Xu G, Zhou L, Bradford P D and Zhang X 2013 *Nano Energy* **2** 976–86
[76] Yang H W, Lee D I, Kang N, Kang W S and Kim S J 2019 *Mater. Res. Lett.* **7** 89–96
[77] Pan Q, Zuo P, Lou S, Mu T, Du C, Cheng X, Ma Y, Gao Y and Yin G 2017 *J. Alloys Compd.* **723** 434–40
[78] Zheng G *et al* 2018 *Adv. Energy Mater.* **8** 1801718
[79] Gu M, He Y, Zheng J and Wang C 2015 *Nano Energy* **17** 366–83
[80] Tusi M M, Brandalise M, Correa O V, Oliveira Neto A, Linardi M and Spinacé E V 2007 *Mater. Res.* **10** 171–5
[81] Tang X *et al* 2018 *ACS Appl. Mater. Interfaces* **10** 5519–26
[82] Moldovan A, Feldmann F, Krugel G, Zimmer M, Rentsch J, Hermle M, Roth-Fölsch A, Kaufmann K and Hagendorf C 2014 *Energy Proc.* **55** 834–44
[83] Xu Z L, Zhang B and Kim J K 2014 *Nano Energy* **6** 27–35
[84] Mehonic A, Buckwell M, Montesi L, Garnett L, Hudziak S, Fearn S, Chapter R, Mcphail D and Kenyon A J 2017 *J. Appl. Phys.* **117** 124505
[85] Gauthier M, Mazouzi D, Reyter D, Lestriez B, Moreau P, Guyomard D and Roué L 2013 *Energy Environ. Sci.* **6** 2145–55
[86] Li X, Wu M, Feng T, Xu Z, Qin J, Chen C, Tu C and Wang D 2017 *RSC Adv.* **7** 48286–93
[87] Sonia F J, Kalita H, Aslam M and Mukhopadhyay A 2017 *Nanoscale* **9** 11303–17
[88] Milenov T and Avramova I 2015 *Opt. Quantum Electron.* **47** 851–63
[89] Xing Y, Shen T, Guo T, Wang X, Xia X, Gu C and Tu J 2018 *J. Power Sources* **384** 207–13
[90] Ferrari A C and Basko D M 2013 *Nat. Nanotechnol.* **8** 235–46
[91] Bonaccorso F, Tan P H and Ferrari A C 2013 *ACS Nano* **7** 1838–44
[92] Agyeman D A, Song K, Lee G H, Park M and Kang Y M 2016 *Adv. Energy Mater.* **6** 1600904
[93] Patze S, Huebner U, Weber K, Cialla-May D and Popp J 2018 *Materials* **11** 325
[94] Merlen A, Buijnsters J G and Pardanaud C 2017 *Coatings* **7** 153
[95] Zhou M, Cai T, Pu F, Chen H, Wang Z, Zhang H and Guan S 2013 *ACS Appl. Mater. Interfaces* **5** 3449–55
[96] Li M, Yu Y, Li J, Chen B, Wu X, Tian Y and Chen P 2015 *J. Mater. Chem.* A **3** 1476–82
[97] Xu C, Lindgren F, Philippe B, Gorgoi M, Björefors F, Edström K and Gustafsson T 2015 *Chem. Mater.* **27** 2591–9
[98] Jerliu B, Hüger E, Dörrer L, Seidlhofer B K, Steitz R, Horisberger M and Schmidt H 2018 *Phys. Chem. Chem. Phys.* **20** 23480–91
[99] Xu Z L, Zhang B, Abouali S, Akbari Garakani M, Huang J, Huang J Q, Heidari E K and Kim J K 2014 *J. Mater. Chem.* A **2** 17944–51
[100] Wu H and Cui Y 2012 *Nano Today* **7** 414–29
[101] Wang F, Chen G, Zhang N, Liu X and Ma R 2019 *Carbon Energy* **1** 219–45
[102] Mukanova A, Nurpeissova A, Urazbayev A, Kim S, Myronov M and Bakenov Z 2017 *Electrochim. Acta* **258** 800–6
[103] Su J, Zhang C, Chen X, Liu S, Huang T and Yu A 2018 *J. Power Sources* **381** 66–71
[104] Fu K, Lu Y, Dirican M, Chen C, Yanilmaz M, Shi Q, Bradford P D and Zhang X 2014 *Nanoscale* **6** 7489–95
[105] Kim H J, Choi S, Lee S J, Seo M W, Lee J G, Deniz E, Lee Y J, Kim E K and Choi J W 2016 *Nano Lett.* **16** 282–8
[106] Zhao J, Lu Z, Liu N, Lee H, Mcdowell M T and Cui Y 2014 *Nat. Commun.* **5** 5088
[107] Chang S, Moon J, Cho K and Cho M 2015 *Comput. Mater. Sci.* **98** 99–104
[108] Zhao J, Lu Z, Wang H, Liu W, Lee H, Yan K, Zhuo D, Lin D, Liu N and Cui Y 2015 *J. Am. Chem. Soc.* **137** 8372–5
[109] Holtstiege F, Bärmann P, Nölle R, Winter M and Placke T 2018 *Batteries* **4** 1–39
[110] Shen C, Fu R, Xia Y and Liu Z 2018 *RSC Adv.* **8** 14473–8
[111] Berhaut C L *et al* 2020 *Energy Storage Mater.* **29** 190–7
[112] Suresh S, Wu Z P, Bartolucci S F, Basu S, Mukherjee R, Gupta T, Hundekar P, Shi Y, Lu T M and Koratkar N 2017 *ACS Nano* **11** 5051–61
[113] Wagner N P, Tron A, Tolchard J R, Noia G and Bellmann M P 2019 *J. Power Sources* **414** 486–94
[114] Ai G *et al* 2016 *J. Power Sources* **309** 33–41
[115] Ren J G, Wu Q H, Hong G, Zhang W J, Wu H, Amine K, Yang J and Lee S T 2013 *Energy Technol.* **1** 77–84
[116] Hu R, Sun W, Chen Y, Zeng M and Zhu M 2014 *J. Mater. Chem.* A **2** 9118–25